

RSC Advances



This is an *Accepted Manuscript*, which has been through the Royal Society of Chemistry peer review process and has been accepted for publication.

Accepted Manuscripts are published online shortly after acceptance, before technical editing, formatting and proof reading. Using this free service, authors can make their results available to the community, in citable form, before we publish the edited article. This *Accepted Manuscript* will be replaced by the edited, formatted and paginated article as soon as this is available.

You can find more information about *Accepted Manuscripts* in the [Information for Authors](#).

Please note that technical editing may introduce minor changes to the text and/or graphics, which may alter content. The journal's standard [Terms & Conditions](#) and the [Ethical guidelines](#) still apply. In no event shall the Royal Society of Chemistry be held responsible for any errors or omissions in this *Accepted Manuscript* or any consequences arising from the use of any information it contains.

Enhanced Visible-Light-Driven Photocatalytic performances using $\text{Bi}_2\text{WO}_6/\text{MS}$ (M= Cd, Zn) heterostructures: Facile synthesis and their photocatalytic mechanisms

Rongfeng Tang, Huaifen Su, Shengxia Duan, Yuanwei Sun, Lei Li, Xianxi Zhang, Suyuan Zeng *
and Dezhi Sun *

Shandong Provincial Key Laboratory of Chemical Energy Storage and Novel Cell Technology,
Department of Chemistry and Chemical Engineering, Liaocheng University, Liaocheng 252059,
China

Corresponding author: Suyuan Zeng and Dezhi Sun. Tel: +86-635-8230614, Fax: +86-635-8230196. Email: drzengsy@163.com, sundezhi@lcu.edu.cn

Abstract:

The formation of type II heterostructure is proved to be an effective method to improve the photocatalytic performance of semiconductors. In this report, a surface functionalization method using 3-mercaptopropionic (MPA) as the surface functionalizing agent was adopted for the fabrication of $\text{Bi}_2\text{WO}_6/\text{MS}$ ($\text{M}=\text{Cd}$ and Zn) heterostructures. The composition and microstructures of the as-prepared heterostructures were characterized by X-ray diffraction (XRD), scanning electron microscopy (SEM), transmission electron microscopy (TEM), high-resolution TEM (HRTEM) and X-ray photoelectron spectroscopy (XPS). The as-prepared $\text{Bi}_2\text{WO}_6/\text{CdS}$ and $\text{Bi}_2\text{WO}_6/\text{ZnS}$ heterostructures exhibit enhanced photocatalytic activities for the degradation of Rhodamine B (Rh B) as compared to pure Bi_2WO_6 , CdS, ZnS nanoparticles and Degussa P25. The enhanced photocatalytic activities of the as-prepared heterostructures may relate to the effective electron-hole separation during the photocatalytic process. A series of scavenger (Benzoquinone for $\text{O}_2^{\cdot-}$, ammonium oxalate for h^+ , AgNO_3 for e^- , and t-BuOH for $\cdot\text{OH}$) were employed to investigate the possible mechanism of the photocatalytic process. The result clearly indicate that the photogenerated holes are the main active species during the photocatalytic process.

Key words: $\text{Bi}_2\text{WO}_6/\text{CdS}$ heterostructures; $\text{Bi}_2\text{WO}_6/\text{ZnS}$ heterostructures, visible-light-driven photocatalysis; scavenger.

1. Introduction

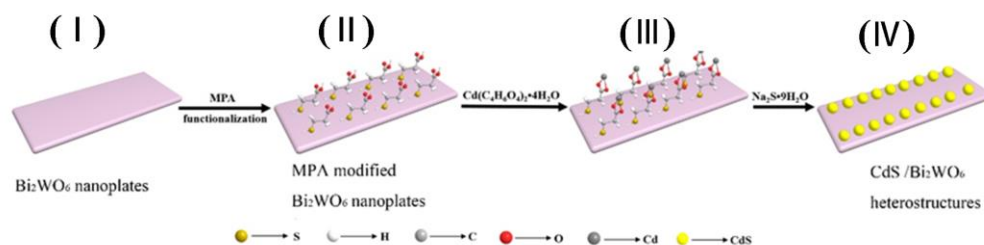
Photocatalysts for the degradation of organic pollutants using solar light energy has attracted increasing interest in the past years because of the growing environment concerns and the energy demand [1–5]. Compared with the traditional methods, semiconductor-based photocatalysis offers a greener route for the elimination of a variety of contaminants, especially for azo dyes [6]. For this purpose, a great number of visible-light-driven photocatalysts have been successfully synthesized, which have been proved to be effective for the elimination of the organic pollutants [7–12]. Among these photocatalysts, Bi_2WO_6 has attracted increasing attention because of its excellent visible-light-driven photo-catalytic activity. The unique layered structure of Bi_2WO_6 favors for the charge transfer process and retards the recombination of holes and electrons during the photo-catalytic process [13], making it an ideal candidate for the photo-degradation of organic pollutants. As a result, a variety of Bi_2WO_6 nano-structures with different morphologies including nest [14], flake-ball [15], disk [16], cage [17], flowers [18–20] have been successfully prepared. Although these Bi_2WO_6 nanostructures

have been found to display strong visible light response, the photocatalytic activity is expected to be further improved to satisfy the large-scale application under visible light irradiation. According to the previous reports, two formidable challenges still remain [21-22]. One centers on the difficult migration and high recombination of photo-generated electron-hole pairs, which will greatly reduce the photocatalytic activity of Bi_2WO_6 . A second entails its wide band gap, which severely precludes the employment of visible light with wavelength longer than $\sim 450\text{nm}$.

It is widely believed that the coupling of two semiconductors is an effective way to enhance the photocatalytic performance, which would lead to a more efficient photoelectron-hole separation or expansion of the spectral absorption range [23-24]. The electrons excited by the visible light would transfer from conduction band of semiconductor with low band gap to the conduction band of Bi_2WO_6 , which will facilitate the charge separation and improve the visible-light photocatalytic activities of the heterostructures dramatically. As a result, a variety of Bi_2WO_6 based heterostructures have been successfully prepared, including $\text{Bi}_2\text{WO}_6/\text{WO}_3$ [25], $\text{Bi}_2\text{WO}_6/\text{Bi}_2\text{S}_3$ [26], $\text{Bi}_2\text{WO}_6/\text{BiOBr}$ [27], $\text{Bi}_2\text{WO}_6/\text{TiO}_2$ [28], $\text{Bi}_2\text{WO}_6/\text{Bi}_2\text{O}_3$ [29] and so on. All of these works clearly indicate that the coupling of another semiconductor is indeed an effective method to improve the photocatalytic activities of Bi_2WO_6 . For example, Huang and co-workers have succeeded in the preparation of layered $\text{Bi}_2\text{WO}_6/\text{BiIO}_4$ heterojunctions by a one-step hydrothermal preparation strategy. The degradation rate for Rh B was almost 34.4 and 4.1 times higher than the corresponding values of BiIO_4 and Bi_2WO_6 , respectively [30]. Fu and co-workers have also reported the preparation of $\text{Bi}_2\text{WO}_6/\text{Ag}_3\text{PO}_4$ hierarchical heterostructures, whose degradation rate for phenol under visible light irradiation was about 1.7 and 1.1 times higher than pure Bi_2WO_6 and Ag_3PO_4 , respectively [31]. However, the synthesis of the Bi_2WO_6 based heterostructure is still a big challenge for the chemists, especially by a simple and economic method.

Recently, the coupling of metal sulfides with other semiconductors has been found to be an effective route for the preparation of photocatalysts with high photocatalytic activities [32-37]. Thus, it is speculated that the sensitization property of metal sulfides will be helpful in overcoming the drawbacks of Bi_2WO_6 and lead to the formation of highly efficient photocatalysts. In this study, two Bi_2WO_6 based heterostructure ($\text{Bi}_2\text{WO}_6/\text{CdS}$ and $\text{Bi}_2\text{WO}_6/\text{ZnS}$) have been successfully prepared using a simple surface functionalization route. Evaluated by the degradation of Rhodamine B (Rh B), the as-formed $\text{Bi}_2\text{WO}_6/\text{MS}$ ($\text{M}=\text{Cd}$ and Zn) heterostructures exhibit enhanced photocatalytic

activities for the degradation of Rh B under visible light irradiation. Based on experimental results and the band gap positions, a possible photodegradation mechanisms of these heterostructures were also systematically investigated.



Scheme 1. Schematic illustration for the synthetic process of $\text{Bi}_2\text{WO}_6/\text{CdS}$ heterostructures.

2. Experimental Section

2.1. Preparations of flower-like Bi_2WO_6 .

All the reagents were of analytical grades and used without further purification. Flower-like Bi_2WO_6 structures was prepared by a hydrothermal process as we have reported previously [38]. In a typical process, 2 mmol $\text{Bi}(\text{NO}_3)_3 \cdot 5\text{H}_2\text{O}$ and 1 mmol $\text{Na}_2\text{WO}_4 \cdot 2\text{H}_2\text{O}$ were dissolved separately in 22.5 mL de-ionized water. Then, the two solutions were mixed under vigorous stirring. The resulting slurries were stirred for 30 min and then transferred into a 50 mL Teflon-lined autoclave. The autoclaves were maintained at 200°C for 12 h and then cooled to room temperature naturally. The precipitates were collected by centrifugation, washed four times with deionizer water and ethanol, and then dried at 60°C for 6 h in vacuum.

2.2 Preparations of $\text{Bi}_2\text{WO}_6/\text{CdS}$ and $\text{Bi}_2\text{WO}_6/\text{ZnS}$ Heterostructures.

For the growth of CdS and ZnS nanoparticles onto flower-like Bi_2WO_6 structures, a surface functionalization route using 3-mercaptopropionic acid (MPA) as the functionalizing agent was adopted [39]. The synthetic process of $\text{Bi}_2\text{WO}_6/\text{CdS}$ heterostructures is illustrated in Scheme 1. In a typical process, 20 μL of MPA was added to the suspension containing 1.0 g Bi_2WO_6 . The suspension was stirred for 4 h at room temperature to complete the surface functionalization of the Bi_2WO_6 surfaces. Afterward, 0.1 g $\text{Cd}(\text{CH}_3\text{COO})_2 \cdot 4\text{H}_2\text{O}$ was added to the above suspension under constant magnetic stirring. After stirring for 2 h, 0.09 g of $\text{Na}_2\text{S} \cdot 9\text{H}_2\text{O}$ was added slowly to the system and stirred constantly for 1 h at room temperature. The solution gradually turned to be faded yellow, which suggest the formation of $\text{Bi}_2\text{WO}_6/\text{CdS}$ heterostructures, and the nominal content of CdS with respect to Bi_2WO_6 is about 23.4% (molar ratio). Subsequently, the resulting product was separated

by centrifugation and washed repeatedly with water and absolute alcohol and then dried in vacuum at 60 °C for 6 h. As for the preparation of Bi₂WO₆/ZnS heterostructure, Cd(CH₃COO)₂•4H₂O added in the second step was replaced by Zn(NO₃)₂•6H₂O, keeping the other reactions conditions unchanged. By calculation, the nominal content of ZnS with respect to Bi₂WO₆ is about 23.5% (molar ratio).

2.3 Preparations of CdS and ZnS nanoparticles.

For comparison purpose, CdS and ZnS nanoparticles were prepared by a simple precipitation method. Take the synthesis of CdS nanoparticles for example, 1.0 g of Cd(CH₃COO)₂•4H₂O was firstly dissolved in 40 mL of deionized water to form a transparent solution. In the next step, 0.9 g Na₂S•9H₂O was added into the above solution and stirred for 1 h at room temperature. Finally, the product was separated by centrifugation, washed repeatedly with deionizer water and ethanol and then dried at 60 °C for 6 h in vacuum. ZnS nanoparticles were synthesized by a similar process during which Zn(NO₃)₂•6H₂O was used as the starting material.

2.4 Sample characterizations.

The phase and composition of the samples were characterized by X-ray powder diffraction (XRD) on a Philips X'Pert Pro Super diffractometer with Cu K α radiation ($\lambda=1.5416 \text{ \AA}$). The XRD pattern was recorded in the 2θ range of 10-70° with scan rate of 0.05 ° s⁻¹. The S-4800 (Hitachi) field emission scanning electron microscope (FESEM) equipped with a GENESIS4000 energy dispersive X-ray spectroscope was applied to observe the size and morphology of the product. The transmission electron microscope (TEM) image was taken on a Hitachi H-7650 transmission microscope, using an accelerating voltage of 120 kV. High-resolution transmission electron microscopy (HRTEM) images were obtained on a JEOL-2010 TEM at an acceleration voltage of 200 kV. X-ray photoelectron spectroscopy (XPS) was recorded on Thermo ESCALAB 250 system with a monochromatic Al K α source with 1486.6 eV of energy, 15 kV of voltage, and 150 W of power. The Brunauer-Emmett-Teller (BET) tests were carried out via a Quantachrome autosorb IQ-C nitrogen adsorption apparatus. All the as-prepared samples were degassed at 150 °C for 4 h prior to nitrogen adsorption measurements. UV-vis diffuse reflectance spectra (DRS) were recorded on a UV-vis spectrometer (Shimadzu UV-2550) by using BaSO₄ as a reference and were converted from reflection to absorbance by the Kubelka-Munk method. The photoluminescence (PL) spectra of the photocatalysts were detected using an F-7000 FL Spectrophotometer.

2.5 Photocatalytic experiments.

In a general process, the photocatalytic activities of the photocatalysts were evaluated by the degradation of rhodamine B (Rh B). In a typical process, 80 mg of the as-synthesized photocatalysts were dispersed in 80 mL 1.0×10^{-5} mol·L⁻¹ rhodamine B (Rh B) solution and then magnetically stirred in the dark for 30 min to reach the adsorption-desorption equilibrium. The solution was then exposed to a 500 W Xe lamp with a cutoff filter ($\lambda > 400$ nm). And the working distance from the Xe lamp to the beaker is kept to be 20 cm. The optical power was measured to be 25.8 mW/cm² during the whole photocatalytic process. To avoid the increase of the temperature during the irradiation process, the beaker containing the dispersion of Rh B and photocatalyst was cooled by circulating water during the whole photocatalysis process. The temperature of the solution was maintained to be 20 °C during the whole process to prevent the thermal catalytic effect. At given irradiation time, adequate aliquots (6 mL) of the suspension were extracted and centrifuged at 9000 rpm to remove the residual photocatalyst for analysis. The concentration of Rh B in the solution was calculated by the intensity of UV-Vis absorption (Agilent Cary 5000E UV-visible spectrophotometer).

2.6 Active species trapping experiments.

To explore the possible photocatalytic mechanism, active species trapping experiments was carried out by using various kinds of scavengers such as Benzoquinone (BQ) (a quencher of O₂^{•-}), ammonium oxalate (AQ) (a quencher of h⁺), AgNO₃ (a quencher of e⁻), and t-BuOH (a quencher of •OH), and the amount of scavenger was 10 mM except BQ, which was 1 mM. The whole process is carried out in the similar way as the photocatalytic experiments.

2.7 Photocurrent measurements.

The ITO glass was cut into 3 cm × 0.7 cm slices and washed with water for two times before being bathed in 1 M NaOH solution for 10 min, and then washed with water several times and dried before use. For the preparation of the photoelectrode, 10 mg of photocatalyst was dispersed in 1 mL of absolute ethanol by ultrasonication firstly. In the next step, 10 μL of the resulting dispersion (10 mg mL⁻¹) was drop-casted onto a piece of ITO slice with a fixed area of 0.7 cm² and dried in air at room temperature to form Bi₂WO₆/MS modified ITO electrode. The photocurrent were measured by using an electrochemical analyzer (CHI660B, Chen Hua Instruments, Shanghai, China) with a standard three-electrode configuration, in which a Pt wire was employed as the counter electrode, a saturated Ag/AgCl electrode as the reference electrode and indium tin oxide (ITO) as the working electrode.

The 500 W Xe lamp was used as the photo source, and the measured optical power on the ITO electrode was determined to be 70 mW/cm². The electrolyte solution of photocurrent was phosphate buffered saline (0.1 mol L⁻¹) and the pH value was adjusted to 7.4.

3. Results and Discussion.

3.1 Sample characterizations.

The addition of MPA in the synthetic process is vital importance for the formation of Bi₂WO₆ based heterostructures. Take the formation of Bi₂WO₆/CdS as an example, no CdS will be observed on the nanoplates of Bi₂WO₆ without MPA (Supporting Information, Figure S1a). To further investigate the effect of MPA, FTIR was employed. Pure MPA was reported to possess several typical peaks centering at 2667, 2573, 1711 and 1411 cm⁻¹, which can be assigned to the O–H ($\nu_{\text{O-H}}$), S–H ($\nu_{\text{S-H}}$), C=O ($\nu_{\text{C=O}}$) and C–O ($\nu_{\text{C-O}}$) stretching bands, respectively. [40-41]. As for the sample obtained by adding MPA into the dispersion of Bi₂WO₆, the peaks corresponding to $\nu_{\text{S-H}}$ disappears (Supporting Information, Figure S1b, black line). Because the pK_a of the thiol moiety is quite high (10.3), the disappearance of S-H peak can't be assigned to the deprotonation of sulfhydryl group in MPA [42]. Meanwhile, the solution pH during the synthetic process is about 6, which also suggest that the MPA added during the synthetic process will not be the sulfur source for the formation of the heterostructures. The disappearance of this peak indicate the coordination interaction between Bi³⁺ and MPA, in which Bi³⁺ is bounded to the sulfhydryl group. When Cd²⁺ is added in to the solution during the synthetic process, the intermediate product was also separated and investigated with FTIR (Supporting Information, Figure S1b, red line). The peaks corresponding to $\nu_{\text{C=O}}$ shift from 1637 to 1560 cm⁻¹, which clearly indicate the coordination interaction between carboxyl group of MPA and Cd²⁺. This kind of coordination interaction favors for the adsorption of Cd²⁺ onto the surfaces of Bi₂WO₆ nanoplates, which is of vital importance for the fabrication of Bi₂WO₆/CdS heterostructures. In the next step, when Na₂S was added, CdS nanoparticles finally formed on the surfaces of Bi₂WO₆ nanoplates. Based on the above experimental results and analysis, the role of MPA molecule can be considered to be a “linker”, which connect the host material and modifiers together, leading to the formation of the Bi₂WO₆/MS (M=Cd and Zn) heterostructures.

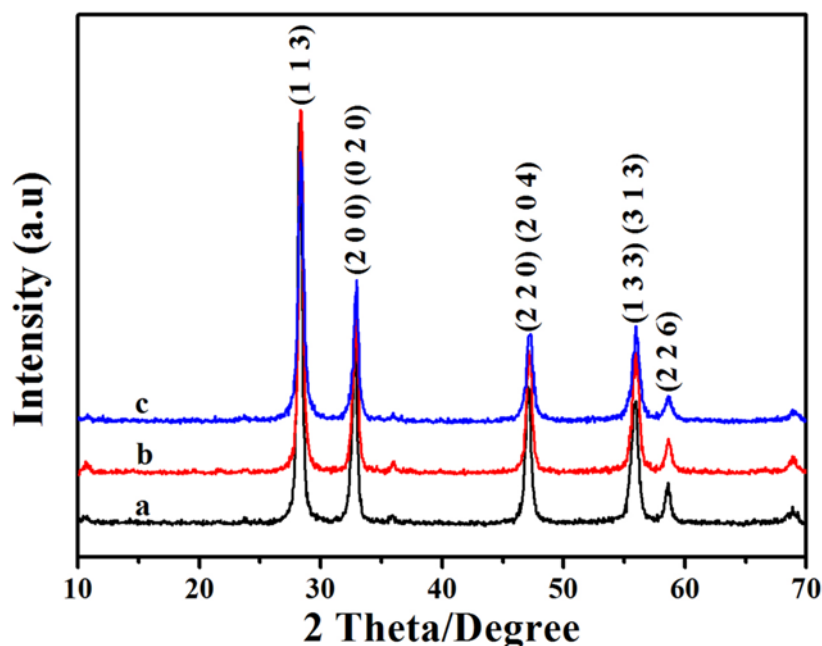


Figure 1. XRD patterns of (a) Bi_2WO_6 , (b) $\text{Bi}_2\text{WO}_6/\text{CdS}$ and (c) $\text{Bi}_2\text{WO}_6/\text{ZnS}$ photocatalysts.

Bi_2WO_6 sample with flower-like structure were prepared by a hydrothermal process at 200°C for 12 hours. The phase purities of the sample is examined by X-ray diffraction (XRD), and the corresponding XRD pattern is displayed as Figure 1a. The diffraction peaks on Figure 1a can be indexed to be the orthorhombic phased Bi_2WO_6 (JCPDS Card, No. 73-1126) [43], indicating the formation of Bi_2WO_6 . The XRD patterns of the samples modified with CdS (BW-Cd) and ZnS (BW-Zn) are displayed as Figure 1b and c. Compared to Figure 1a, no obvious difference can be observed on these two XRD patterns. Although no peak corresponding to CdS or ZnS is detected on the XRD pattern, the existence of CdS or ZnS can't be precluded. This phenomenon may be related to the small amount of CdS or ZnS and their high dispersion in samples [44]. Meanwhile, the synthetic processes were carried out under room temperature, which may lead to the poor crystallinities of MS (M=Cd or Zn). The poor crystallinities of MS would make them difficult to be detected by the XRD examination. To verify the existence of CdS and ZnS in samples BW-Cd and BW-Zn, the chemical compositions of the as-prepared composite photocatalysts were further investigated using X-ray fluorescence (XRF). The results of XRF clearly indicate the existence of CdS and ZnS in sample BW-Cd and BW-Zn. For sample BW-Cd, the atomic ratio between Bi, W, Cd and S is determined to be 2:1:0.18:0.18. While for sample BW-Zn, the corresponding value is determined to be 2:1:0.14:0.14.

The chemical state of the constituent elements for the as-obtained two samples (BW-Cd and BW-Zn) were further investigated by XPS analysis, which is based on the limited escape depth of electrons

with relatively low kinetic energy and reveals information on the topmost few angstroms of the surface [45]. The peak positions in all of the XPS spectra were calibrated with C 1s at 284.60 eV. Figure 2a is the overall XPS spectrum of sample BW-Cd, which clearly indicates the formation of $\text{Bi}_2\text{WO}_6/\text{CdS}$ heterostructure. Fig. 2b-c are the high resolution XPS spectra of S 2s and Cd 3d, respectively. The binding energy centering at 226.4 eV can be assigned to S 2s. Meanwhile, Cd 3d exhibits characteristic peaks at 411.95 and 405.2 eV, corresponding to Cd 3d_{3/2} and Cd 3d_{5/2}. Two peaks centering at 158.85 eV and 164.15 eV can be ascribed to Bi 4f_{7/2} and Bi 4f_{5/2} [46] (Supporting Information, Figure S2a). And the peaks centering at 37.2 and 35.05 eV correspond to W 4f_{5/2} and W 4f_{7/2} [47,13a], respectively (Figure S2b). The formation of $\text{Bi}_2\text{WO}_6/\text{ZnS}$ heterostructure can be also verified by the XPS investigation of sample BW-Zn, which clearly indicate the existence of Bi, W, Zn and S in sample BW-Zn (Figure 2d). The peaks locating at 225.8 eV (shown in Fig. 2e) and 1021.75 eV (shown in Fig. 2f) belong to S 2s and Zn 2p peaks [48], respectively. Peaks centering at 37.45 and 35.3 eV, as shown in Figure S2c, correspond to W 4f_{5/2} and W 4f_{7/2}. The binding energies for Bi 4f_{7/2} and Bi 4f_{5/2} are 159 and 164.3 eV, which can be observed in Figure S2d. For sample BW-Cd, the atomic ratio of Bi : W : Cd : S is determined to be 2 : 1 : 0.35 : 0.35. While for sample BW-Zn, the corresponding atom ratios of Bi : W : Zn : S is determined to be 2 : 1 : 0.22 : 0.22. It should be noted that the content of CdS or ZnS determined by the XPS are much larger than the corresponding values determined by the XRF investigation, which suggest that MS (M=Cd, Zn) nanoparticles is mainly dispersed on the surfaces of flower-like Bi_2WO_6 structures. Meanwhile, the content of CdS determined by XPS is much larger than the corresponding value of ZnS This phenomenon can be attributed to the different measure modes between XRF and XPS. The And combined with the value obtained from the two techniques, it can indicate that the.

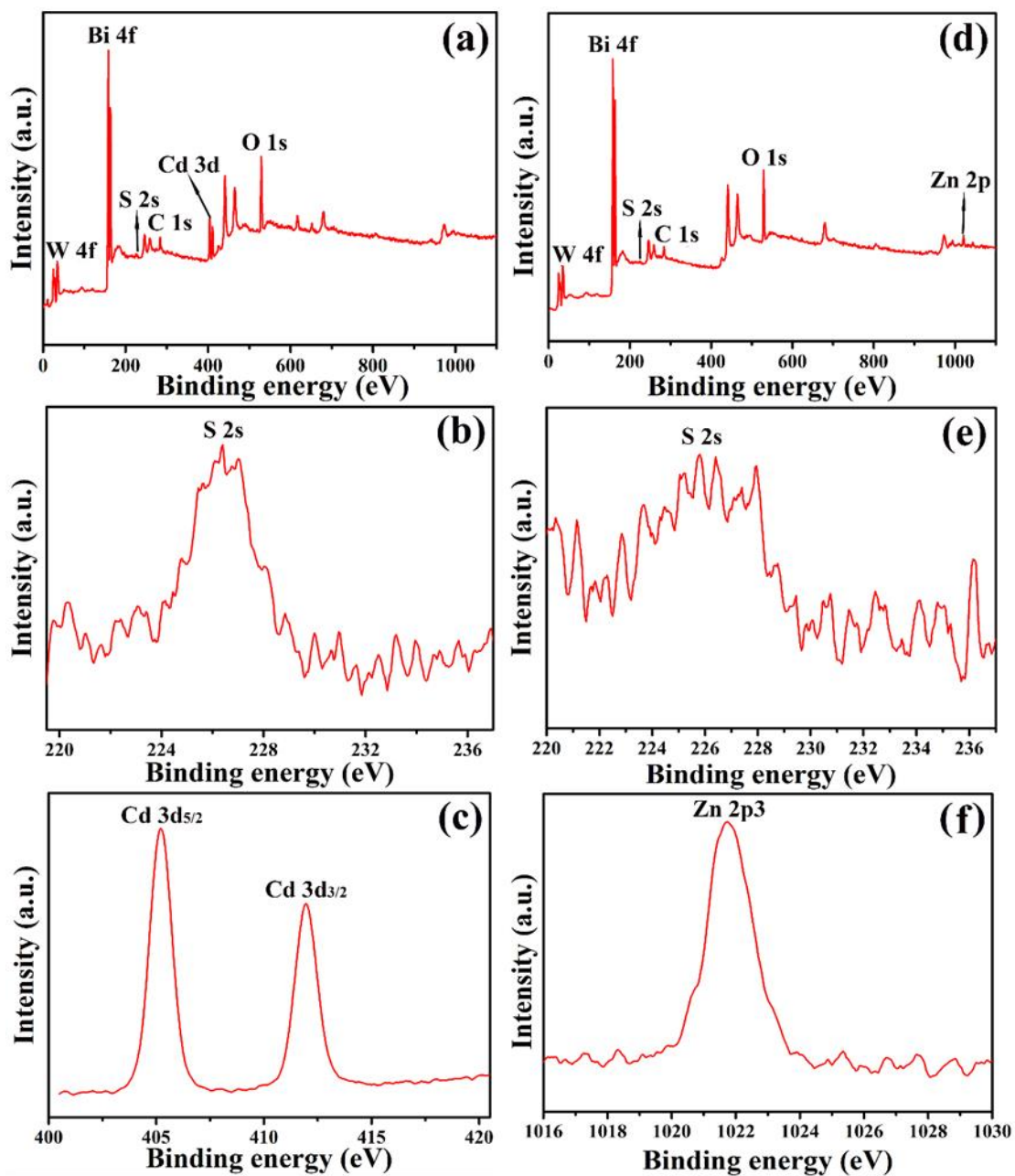


Figure 2. XPS analysis of (a) $\text{Bi}_2\text{WO}_6/\text{CdS}$ sample, (b) S 2s, (c) Cd 3d, (d) $\text{Bi}_2\text{WO}_6/\text{ZnS}$ sample, (e) S 2s, (f) Zn 2p.

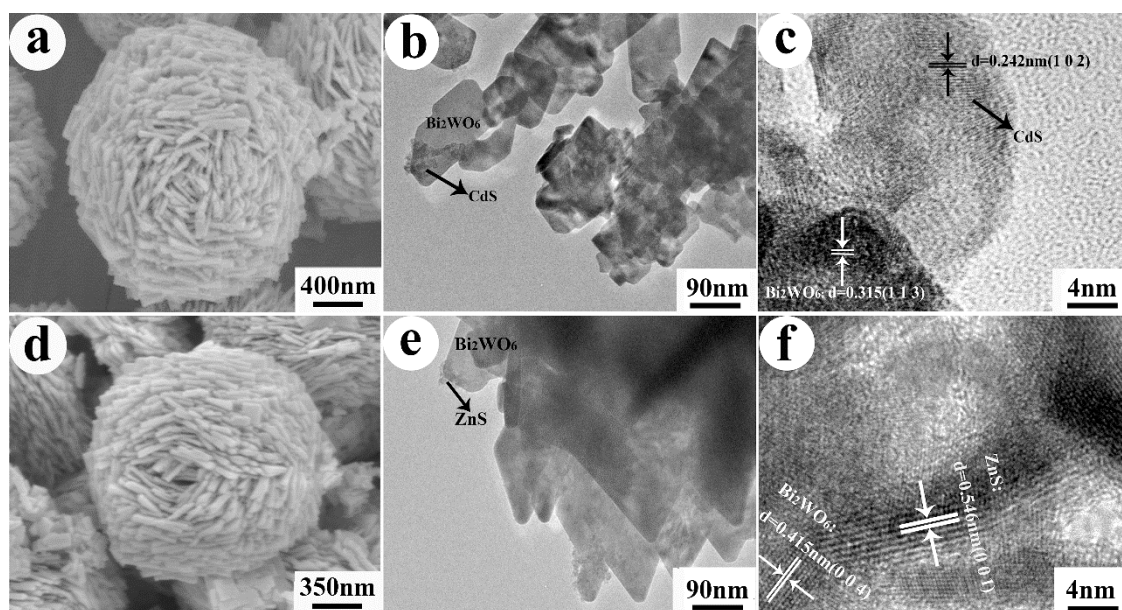


Figure 3. (a) SEM, (b) TEM and (c) HRTEM images of sample BW-Cd; (d) SEM, (e) TEM and (f) HRTEM images of sample BW-Zn.

The morphologies and microstructures of samples BW-Cd and BW-Zn were further investigated by SEM, TEM and HRTEM, and the corresponding results are shown in Figure 3. Figure 3a is the SEM image of sample BW-Cd, which clearly indicate that the sample is composed of flower-like microstructures with diameter of about 2.0 μm , which agrees well with the microstructure of bare Bi_2WO_6 in our previous report [38]. Figure 3b is the high-magnification TEM image of the Bi_2WO_6 nanoplates, suggesting the existence of small nanoparticle on the surfaces of these nanoplates. The sizes of these nanoparticles is about 5-10nm. These small nanoparticles can be designated to be CdS according to the EDS analysis (Supporting Information, Figure S3a). To gain further insight into the detailed structure of sample BW-Cd, HRTEM was employed. Figure 3c is the HRTEM image of sample BW-Cd, which clearly indicate the formation of the $\text{Bi}_2\text{WO}_6/\text{CdS}$ heterostructure. The typical lattice spacing, being determined to be 0.315 nm, is consistent with the (1 1 3) planes of Bi_2WO_6 . The lattice spacing taken on the tiny nanocrystals is about 0.242nm, which is consistent with the (1 0 2) planes of CdS (JCPDS NO. 89-2944). Figure 3d-f shows the SEM, TEM, and HRTEM images of $\text{Bi}_2\text{WO}_6/\text{ZnS}$ heterostructures, which suggest that the existence of ZnS nanoparticles on the surfaces of Bi_2WO_6 nanoplates. Figure 3f is the HRTEM image of sample BW-Zn, which clearly suggest the formation of $\text{Bi}_2\text{WO}_6/\text{ZnS}$ heterostructures. The typical lattice spacing, being determined to be 0.415 nm, is consistent with the (0 0 4) planes of Bi_2WO_6 . The lattice spacing taken on the tiny nanocrystals is about 0.546 nm, which is consistent with the (0 0 1) planes of ZnS (JCPDS NO.80-

0020).

The BET specific surface areas of Bi₂WO₆, BW-Cd and BW-Zn were determined by nitrogen adsorption BET method. And the measurement indicate that the specific surface area of pure Bi₂WO₆, BW-Cd and BW-Zn were about 13.6, 13.9 and 13.7 m² g⁻¹, respectively. No obvious change in BET surface area (as displayed in Supporting Information Figure S4) has been observed among these three samples, which uncovered that the surface area may not be the influencing factor for the different photocatalytic performances of BW-Cd and BW-Zn.

The optical properties of the as-prepared photocatalysts are investigated using the UV-vis diffuse reflectance spectrum (DRS) (Figure 4a and c). Bare Bi₂WO₆ exhibit fundamental absorbance edge at 450 nm because of the intrinsic band-gap transition [49], and the absorbance edge of bare CdS and ZnS is at ~540nm and ~338nm, respectively. The adsorption edge of the sample BW-Cd is at 477nm, which lies between the absorbance edges between Bi₂WO₆ and CdS. Compared with bare Bi₂WO₆, the absorbance edge of sample BW-Cd has an obvious red shift because of the introduction of CdS onto the Bi₂WO₆ nanoplates. As a result, the colors of samples BW-Cd changes from white to yellow (inset of Figure 4a), resulting from the interfacial interactions between Bi₂WO₆ and CdS. As for sample BW-Zn, the absorbance edge is determined to be 575 nm, which show obvious red shift as compared to bare Bi₂WO₆ and ZnS. Liu and co-workers have investigate the optical property of ZnO/ZnAl₂O₄ heterostrucures [50], whose aborbance edge also exhibit obvious red shift as compared to both ZnO and ZnAl₂O₄. This kind of change is attributed to the middle band gap between the CB bottom of ZnO and the VB top of ZnAl₂O₄. In our synthesis, the red shift of absorbance edge for sample BW-Zn could also be attributed to the middle band gap formed between the CB bottom of Bi₂WO₆ and the VB top of ZnS, which is mainly caused by the interfacial interaction between ZnS and Bi₂WO₆. This phenomena have also been reported by several groups for a variety of semiconductor heterostructures such as Bi₂MoO₆/TiO₂ [51], and TiO₂/MMT [52].

The optical band gaps of the as-form heterostructures can be calculated using the Tauc plot, which is described as follows: [53]

$$(\alpha h\nu)^{\frac{1}{n}} = A(h\nu - E_g)$$

where h is the Planck's constant, ν is the frequency of vibration, α is the absorption coefficient, E_g is the band gap of the semiconductor. Among them, n is determined from the type of optical transition

of a semiconductor, and the value of n for the direct semiconductor is $1/2$, while for indirect transition, $n = 2$ [39]. By calculation, n is determined to be $1/2$ for the as-formed heterostructures. And the band gaps of Bi_2WO_6 , CdS, ZnS, BW-Cd and BW-Zn were estimated to be 3.08, 2.33, 3.78, 2.74, and 2.86 eV, respectively (Figure 4b and d).

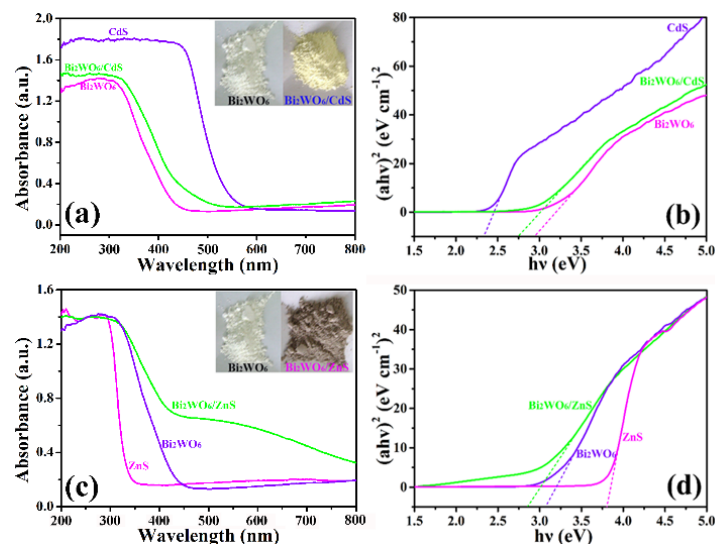


Figure 4. (a) UV-vis absorption spectra of Bi_2WO_6 , CdS and BW-Cd, and (b) Kubelka–Munk plot for band gap calculation of Bi_2WO_6 , CdS, and BW-Cd. The inset in (a) shows the snapshots of Bi_2WO_6 and BW-Cd samples; (c) UV-vis absorption spectra of Bi_2WO_6 , ZnS and BW-Zn, and (d) Kubelka–Munk plot for band gap calculation of Bi_2WO_6 , ZnS, and BW-Zn. The inset in (c) shows the snapshots of Bi_2WO_6 and BW-Zn samples.

Based on the result of DRS, the band edge positions of the as-prepared semiconductors can be theoretically predicted using the electronegativity concept [54–55]. The CB and VB potentials of the semiconductor at the point of zero charge can be calculated by the following equation:

$$E_{CB} = X + E_0 - 0.5E_g$$

and

$$E_{VB} = E_{CB} + E_g$$

where E_g represents the band gap energy of the semiconductor, E_{CB} is the conduction band potential, E_{VB} is the valence band potential, E_0 is scale factor relating to the reference electrode redox level to the absolute vacuum scale ($E_0 = -4.5$ eV for normal hydrogen electrode), and X is the electronegativity of the semiconductor, which is defined as the geometric average of the absolute electronegativity of the constituent atoms. The calculated CB and VB potential of Bi_2WO_6 , CdS, ZnS, BW-Cd, BW-Zn are shown in Table 1. The band gap position of bare Bi_2WO_6 is measured to be 3.08

eV, and the E_{CB} and E_{VB} are calculated to be 0.36 eV and 3.44 eV, respectively. For CdS and ZnS nanoparticles, both the values of E_{CB} and E_{VB} are lower than the corresponding values of Bi_2WO_6 , corresponding to the type-II band gap alignment. This kind of band gap alignment will favor for the separation of electrons and holes during the photocatalytic process and lead to the enhanced photocatalytic activities for the heterostructures.

Table 1. Calculated Values of Band gap, Conduction band (CB) and Valence band (VB) of sample Bi_2WO_6 , CdS, ZnS, BW-Cd and BW-Zn.

Sample	Band gap (eV)	Conduction band (eV)	Valence band (eV)
Bi_2WO_6	3.08	0.36	3.44
CdS	2.33	-0.56	1.76
ZnS	3.78	-1.12	2.66
Bi_2WO_6/CdS	2.74	0.36 (Bi_2WO_6) -0.56 (CdS)	3.44 (Bi_2WO_6) 1.76 (CdS)
Bi_2WO_6/ZnS	2.86	0.36 (Bi_2WO_6) -1.12 (ZnS)	3.44(Bi_2WO_6) 2.66(ZnS)

3.2. Visible-Light-Driven Photocatalytic Activities.

Dyes are pervasive commercial chemicals which have arisen unique environmental problems [56-57]. So it is imperative to remove them before draining them to the environment. Compared to technologies involving physical or biological treatments [58-59], semiconductor-based photocatalysis can achieve significant organic dye pollutant degradation, which is considered as an alternative treatment strategy to solve the environmental problems successfully. To investigate the photocatalytic activities of the as-prepared heterostructures, rhodamine B (Rh B) is chosen as the target pollutant. For comparison purpose, the blank experiment (without photocatalysts), the photocatalytic activities of bare Bi_2WO_6 , CdS nanoparticles, ZnS nanoparticles and Degussa P25 were also investigated. The photodegradation efficiencies of Rh B over BW-Cd, BW-Zn, bare Bi_2WO_6 , CdS, ZnS, Degussa P25 and the blank experiment under visible light are shown in Figure 5a. The blank experiment shows that RhB molecules are very stable and the photolysis is negligible. In addition, both of the as-formed heterostructures (BW-Cd and BW-Zn) display enhanced photocatalytic activities as compared to bare Bi_2WO_6 , CdS nanoparticles and ZnS nanoparticles. The photocatalytic activities among these samples follow the sequence: BW-Cd>BW-Zn> Bi_2WO_6 >P25>CdS>ZnS. Among these samples, sample BW-Cd exhibits the highest photocatalytic activity toward the degradation of Rh B under visible light, and almost 98.7% of the

Rh B can be degraded in 90 min (Figure 5b). The photocatalytic activity of sample BW-Zn is a little poorer than sample BW-Cd and 87.1% of the Rh B can be degraded after irradiating for 90 minutes (Figure 5b). Considering the fact that the two samples possess the similar BET surface areas, the difference in photocatalytic activities may relate to the different band gaps of the two heterostructures. ZnS nanoparticles exhibit the lowest photocatalytic activity, which may result from its large band gap. According to the band gap calculation above, the band gap of ZnS is 3.78 eV, indicating the poor absorbance of light in the visible region. Although the band gap of P25 is also large (3.2 eV), P25 shows a notably higher photoactivity than ZnS. Besides the band gap, the photocatalytic activity of semiconductor is also greatly influenced by a series of factors, such as BET surface areas and crystallinity [60-61]. Figure S5 are the XRD patterns of the as-obtained ZnS nanoparticles and P25, which clearly indicate that the ZnS nanoparticles are poorly crystallized than P25. The difference in the crystallinity could also be reflected by the corresponding SAED pattern taken on these two sample. The poor crystallinity of ZnS nanoparticles could be verified by the ring-like ED pattern. Meanwhile, the BET surface areas of P25 and ZnS nanoparticles are determined to be $50.4 \text{ m}^2 \cdot \text{g}^{-1}$ and $21 \text{ m}^2 \cdot \text{g}^{-1}$, which shows that P25 possess a much larger surface area than the ZnS nanoparticles. So the difference in photocatalytic activities between P25 and ZnS nanoparticles could be attributed to their different crystallinities and surface areas.

As the band gap of P25 is large, it can be anticipated that the photocatalytic activity under visible light will be handicapped. To compare it with BW-MS (M=Cd or Zn), the Xe lamp was replaced by mercury lamp to offer useful photons for both P25 and BW-M systems. The photocatalytic activities sequence among the three samples follow the sequence: P25>BW-Zn>BW-Cd, which is in the opposite sequence as compared to the photocatalytic activities under visible light (Fig. S6). Therefore, it can be concluded that the as-synthesized BW-MS (M=Cd or Zn) is a good visible-light responsive but not a good UV-light responsive photocatalyst.

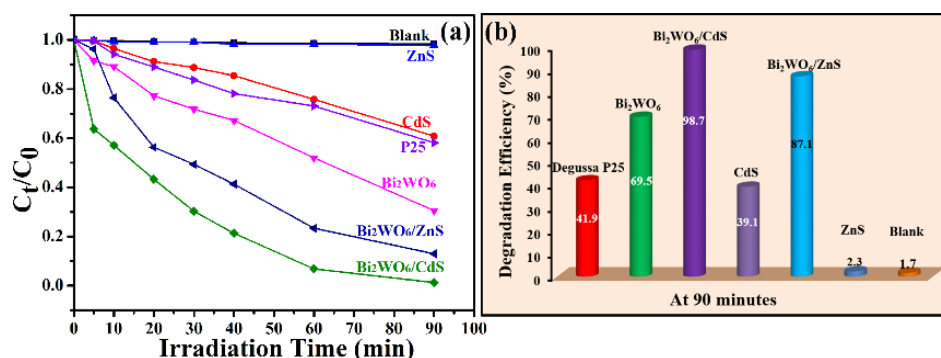


Figure 5. (a) Photocatalytic performance at different time intervals; (b) Degradation efficiency of Blank, Bi₂WO₆, CdS and ZnS nanoparticles, Degussa P25, Bi₂WO₆/CdS and Bi₂WO₆/ZnS heterostructures for the degradation of Rh B solution under visible light irradiation.

To quantitatively understand the reaction kinetics of Rh B degradation in our experiments, Langmuir-Hinshelwood model was employed. This model is well-established for photocatalytic experiments when the concentration of the organic pollutant is in the millimolar range [62], which is expressed as follows:

$$-\ln \frac{C}{C_0} = kt$$

where C_0 is the initial concentration of Rh B (mol L^{-1}), C is the concentrations of pollutant in solution at desired time, and k is the apparent first-order rate constant. The apparent rate constant k is calculated to be 0.04633 and 0.0230 min^{-1} for samples BW-Cd and BW-Zn, respectively (Figure 6). The photodegradation efficiency and apparent rate constant k of all the samples are summarized in Table 2. The photodegradation rate for sample BW-Cd and BW-Zn is 3.72 and 1.85 times than bare Bi₂WO₆, which can be attributed to the effective electron-hole separations at the interfaces of the two semiconductors.

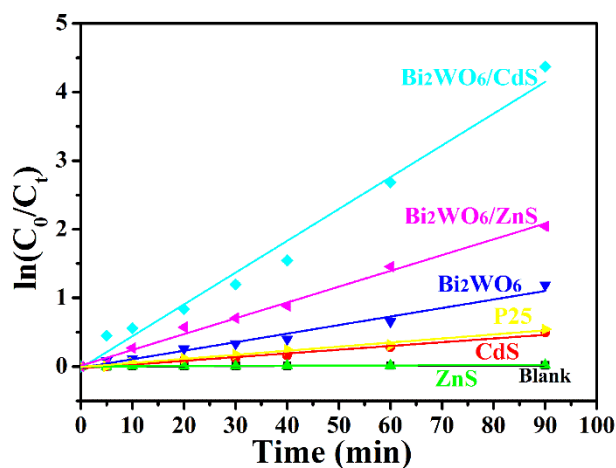


Figure 6. Plot of $\ln(C_0/C)$ as a function of visible irradiation time for photocatalysis of Rh B solution containing: Blank, Bi_2WO_6 , CdS and ZnS nanoparticles, Degussa P25, $\text{Bi}_2\text{WO}_6/\text{CdS}$ and $\text{Bi}_2\text{WO}_6/\text{ZnS}$ heterostructures under visible light irradiation.

Table 2. Photocatalytic efficiency and Rate constant of Bi_2WO_6 , CdS, ZnS, P25, BW-Cd and BW-Zn.

sample	Photocatalytic efficiency	Rate constant (min^{-1})
Bi_2WO_6	69.5%	1.244×10^{-2}
CdS	39.1%	5.420×10^{-3}
ZnS	2.3%	2.472×10^{-4}
P25	41.9%	5.940×10^{-3}
$\text{Bi}_2\text{WO}_6/\text{ZnS}$	87.1%	2.301×10^{-2}
$\text{Bi}_2\text{WO}_6/\text{CdS}$	98.7%	4.633×10^{-2}
Blank(No photocatalyst)	1.7%	1.862×10^{-4}

The stability of the $\text{Bi}_2\text{WO}_6/\text{MS}$ (M=Cd or Zn) heterostructures were also investigated by the degradation of RhB under visible-light irradiation (shown in Fig. S7). It should be noted that the photocatalytic activity of BW-Cd and BW-Zn catalyst exhibit obvious loss after five cycles. And the photodegradation efficiency decreased to 86.2% and 90% of their initial photocatalytic efficiency, respectively. According to the previous report, both CdS and ZnS are easily suffered from photocorrosion in aqueous media containing oxygen when exposed to visible light [63-66]. Thus, the decrease in the photocatalytic activities of the as-obtained heterostructures may result from the photocorrosion of the metal sulfide during the photocatalytic process.

The improved photocatalytic activities of BW-Cd and BW-Zn is closely to the enhanced separation efficiency of photogenerated electrons and holes. To clarify this view, the photocurrent and photoluminescence spectra of bare Bi_2WO_6 , BW-Cd and BW-Zn are investigated. Electrons in the conduction band and holes in the valence band were generated in the semiconductor under irradiation. As well known, the separation efficiency of electrons and holes play a crucial role during the photocatalytic reaction [67]. A higher photocurrent indicate the presence of photogenerated electrons and holes longer lives and hence the higher the photocatalytic activity can be achieved [68]. From the I-t curves (shown in Figure 7), it can be seen that the BW-Cd and BW-Zn exhibit higher transient photocurrent density than bare Bi_2WO_6 , which indicate an enhanced photo-induced electrons and holes separation efficiency. And the enhancement in the separation efficiency of electrons and holes for these two samples is higher than bare Bi_2WO_6 , resulting from the interactions between Bi_2WO_6

and MS (M=Cd and Zn).

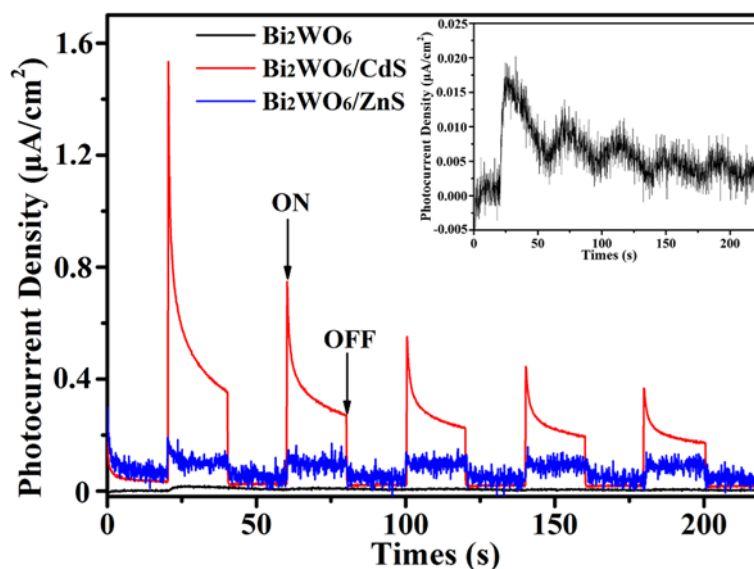


Figure 7. Transient photocurrent response for the sample Bi_2WO_6 , BW-Cd, and BW-Zn. The inset in Figure 7 shows the amplifying photocurrent of bare Bi_2WO_6 .

Photoluminescence (PL) spectrum is also a useful technique to survey the separation efficiency of the photogenerated charge carriers in a semiconductor, because the PL emission mainly results from the recombination of free carriers [69]. In general, lower PL intensity means lower recombination rate of the electron-hole pairs under light irradiation. The PL spectra (excited at 300 nm) of bare Bi_2WO_6 , BW-Cd and BW-Zn at room temperature is shown in Figure 8. It can be found that the PL emission intensities of samples BW-Cd and BW-ZnS composite are dramatically weakened as compared to bare Bi_2WO_6 . Sample BW-Cd exhibits the lowest emission peaks, which indicates that the formation of the heterostructures between Bi_2WO_6 and CdS would greatly facilitate the separation of the photo-generated charge carriers. As a result, the photocatalytic activity of the BW-Cd was greatly enhanced, and that is the reason why sample BW-Cd exhibits the highest photocatalytic activity.

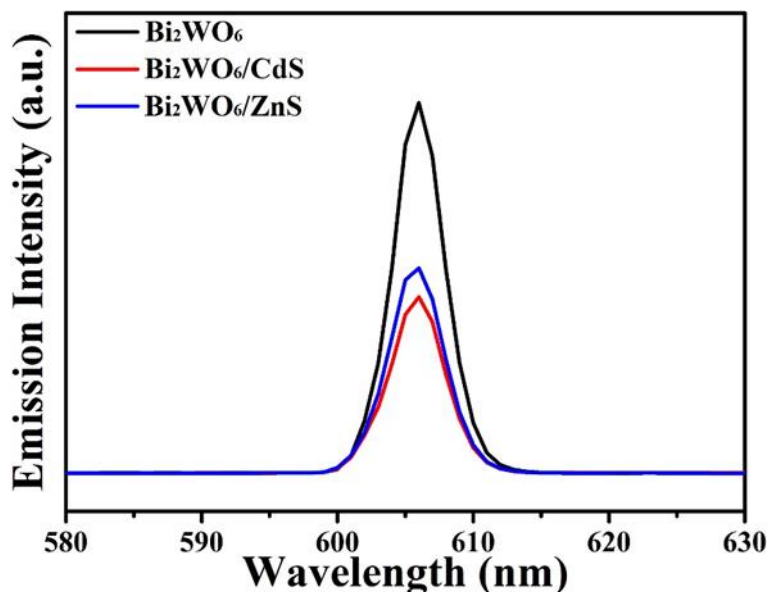


Figure 8. PL spectra of sample Bi_2WO_6 , BW-Cd, and BW-Zn.

3.2. Mechanism of Photocatalysis.

As for the photodecomposition process of RhB, two photocatalytic mechanisms are generally proposed. One is achieved by the degradation of the conjugated structure via a photocatalytic process [70], during which a decrease of the absorption band without shifting of the maximum absorbance wavelength at 555 nm could be observed. The second pathway is really a photosensitized process, during which the degradation of RhB occurs via the N-deethylation of RhB in a stepwise process. To be specific, RhB initially tetra-ethylated ($\lambda_{\text{max}} = 555$ nm) becomes tri-, di-, mono-, and no-ethylated (λ_{max} is, respectively, 539, 522, 510, and 498 nm) [71-73]. And this process is usually featured by the blue shifting of the absorption band. According to the absorption spectra variation of RhB upon irradiation with the visible light in the presence of BW-Cd and BW-Zn (Supporting Information, Figure S8), the occurrence of the photosensitization process could be confirmed. To figure out the main driving force in the photocatalytic process, a series of comparative experiments were carried out. In the first step, a 510 nm cutoff filter was employed during the whole photocatalytic process, which could only allow the transmission of light with wavelength longer than 510nm. In this region, both BW-Cd and BW-Zn can't be effectively excited, and the photocatalytic process mainly relate to the photosensitized process. The photodegradation efficiency of BW-Cd sharply decreased when the 510nm cutoff filter was employed, and only 5.4% of Rh B was degraded in 90 minutes. As for sample BW-Zn, the photodegradation efficiency can reach to 77% in 90 minutes, which is a little smaller than the corresponding value when the 400 cutoff filter was employed. This result clearly demonstrate

that the photodecomposition of Rh B over BW-Cd is mainly driven by the first pathway (photocatalytic process). While for sample BW-Zn, the photodecomposition of Rh B is a photosensitization process indeed. So, although both photocatalytic process and photosensitization process exist during the photodecomposition of RhB, the influence of these two pathways are totally different for this two samples. To further clarify our view, 4-chlorophenol (4-CP) was chosen as the target pollutant, because it has no light absorption in the visible-light region and no photosensitization in the visible light region. The initial concentration of 4-CP was $7.5 \times 10^{-5} \text{ mol} \cdot \text{L}^{-1}$, and the dosage of photocatalyst was same to the typical photocatalytic experiments. The photocatalytic of the three sample bare Bi_2WO_6 , BW-Zn and BW-Cd over 4-CP were shown in Figure 7b, which clearly indicate that all of the three samples exhibit photocatalytic activities under visible light. Among the three sample, BW-Cd exhibits the highest photocatalytic activity. It should be noted that the photocatalytic activity of BW-Zn exhibits much lower photocatalytic activity as compared to BW-Cd, which also suggest that the photosensitization process play a key role in the photodecomposition process.

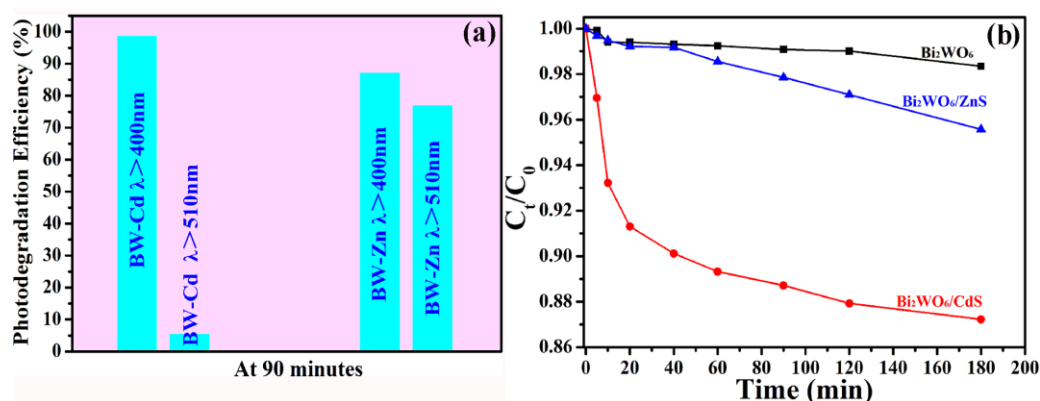


Figure 7. (a) Photodegradation efficiency of BW-Cd and BW-Zn under different visible light ($\lambda > 510\text{nm}$ and $\lambda > 400\text{nm}$) irradiation; (b) visible-light photodegradation of 4-CP in the presence of Bi_2WO_6 , BW-Cd and BW-Zn.

In order to reveal the active species during the photocatalytic process, the trapping experiments were conducted. A series of quenchers such as Benzoquinone (BQ, scavenger for $\text{O}_2^{\cdot-}$), ammonium oxalate (AQ, scavenger for h^+), AgNO_3 (scavenger for e^-), and t-BuOH (scavenger for $\cdot\text{OH}$) were introduced to the Rh B solution before the addition of photocatalyst to ascertain the ruling active species [74], and the corresponding results are shown in Figure 9. The amount of these quenchers is 10 mM except for the BQ, which is 1 mM to avoid the reaction with Rh B. For both the two heterostructures, the addition of t-butanol (hydroxyl radicals scavenger) only cause a small decrease

on the photodegradation rate of Rh B, indicating that hydroxyl radicals are not the driving force for the degradation of Rh B. On the contrary, the introduction of ammonium oxalate (the holes scavenger) cause an inhibition phenomenon on the photodegradation of Rh B, suggesting that the photo-generated holes play vital roles in the degradation of Rh B. Meanwhile, the photodegradation of Rh B was also substantially reduced by the addition of AgNO_3 (electrons scavenger) and BQ (superoxide radical anions scavenger), indicating that both electron and superoxide radical anions also exist in the solution.

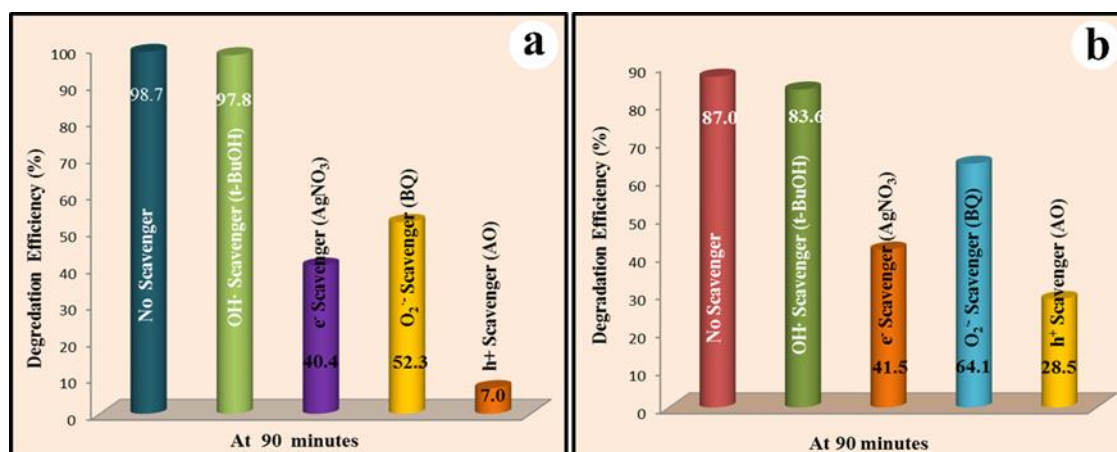
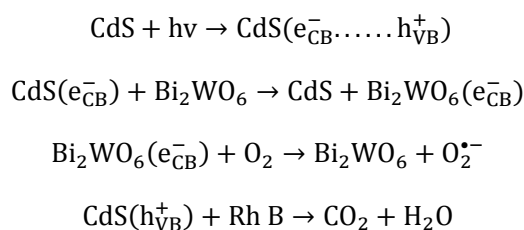
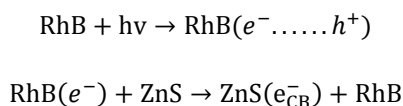


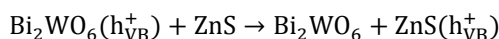
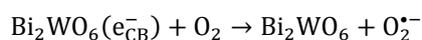
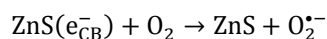
Figure 9. Effects of a series of scavengers on the photodegradation efficiency of Rh B using sample (a) BW-Cd, and (b) BW-Zn.

For sample BW-Cd, the enhanced photocatalytic performance can be well ascribed to the interfacial interaction between CdS and Bi_2WO_6 . And the process of photodegradation can be described as follows:

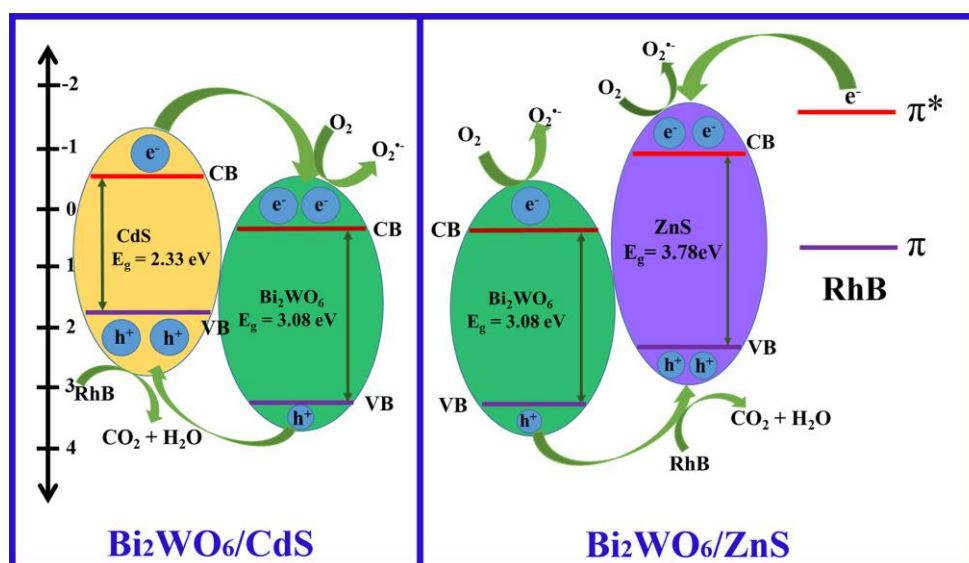


While for BW-Zn, the photosensitization process play an important role in the photocatalytic process. Besides the bandgap coupling of the two semiconductors, RhB can also absorb incident photon flux owing to the intermolecular $\pi-\pi^*$ transition. So the photodegradation process of BW-Zn may be different from sample BW-Cd, which could be described as follows:





where e_{CB}^- and h_{VB}^+ stand for the electron in the conduction band and hole in the valence band, respectively.



Scheme 2. Schematic diagram showing separation of photo-generated charge carriers in sample BW-Cd and BW-Zn.

Based on the above experimental results, the schematic diagrams for the photocatalytic process in the presence of BW-Cd and BW-Zn are presented in Scheme 2. When BW-Cd is irradiated, electrons are excited from the valence band (VB) of CdS to its conduction band (CB). Then, the CB-electrons of CdS could easily transfer to the CB of Bi_2WO_6 , driven by the decrease in potential energy. This process could facilitate their participation in an electron reduction reaction of oxygen to activate molecular oxygen (e.g., the formation of superoxide radical anion). As a result, the recombination of electron-hole pairs were efficiently inhibited and the lifetime of charge carriers were prolonged, which would lead to the enhanced photocatalytic performances of the as-formed heterostructures.

As for BW-Zn, the photocatalytic mechanism is different to BW-Cd. Because of the large band gap of ZnS, ZnS can't be excited under visible light. So, when BW-Zn was irradiated with visible light, electrons are easily excited from the VB of Bi_2WO_6 to its CB. Then the photo-generated holes

will transfer to the VB of ZnS because of direction of inter-built electric field. Meanwhile, RhB dye could absorb the incident photon flux upon visible light irradiation. Then, the photo-generated electrons were transferred to the excited state of the dye owing to the intramolecular π - π^* transition and the dyes were oxidized. The photoelectrons of the excited state were immediately injected into the conducting band of Bi_2WO_6 . The photoelectrons in the CB were then captured by O_2 , and the succeeding reactions can lead to the decomposition of the dyes. Because of the formation of heterostructures, the separation efficiency of photo-generated electrons and holes are greatly enhanced, which will lead to the fast decomposition of RhB in our experiment.

4. Conclusions.

In this report, the $\text{Bi}_2\text{WO}_6/\text{CdS}$ and $\text{Bi}_2\text{WO}_6/\text{ZnS}$ heterostructures was successfully prepared by a surface functionalization method using 3-mercaptopropionic (MPA) as the surface functionalizing agent. The formation of these type II heterostructure is proved to be an effective method to improve the photocatalytic performance of the Bi_2WO_6 . And the photodegradation efficiency of sample BW-Cd and BW-Zn for RhB was approximately 3.72 and 1.85 times higher than bare Bi_2WO_6 , respectively. The enhanced photocatalytic activities of the as-obtained heterostructures could be attributed to the facilitated interfacial charge transfer and inhibited electron-hole recombination, which has been confirmed by the photocurrent and PL measurement. The trapping experiments indicate the dominant active species in the photocatalytic process are photo-generated holes. Based on the experimental results, the photocatalytic mechanisms for samples BW-Cd and BW-Zn are proposed. Thus, these novel heterostructured materials are supposed to have potential applications in waste water treatment.

5. Supporting informations.

EDS spectra and BET spectra for the two heterostructures, XPS pattern of Bi 4f and W 4f of BW-MS sample are provided in supporting information.

6. Acknowledgement.

This work was supported by the National Natural Science Foundation of China (Grant No. 21373106) and Program for Scientific Research Innovation Team in Colleges and Universities of Shandong Province.

References:

[1] A. Hagfeldt and M. Gratzel, *Chem. Rev.*, 1995, **95**, 49-68.

- [2] Z. G. Zou, J. H. Ye and K. Sayama, *Nature*, 2001, **414**, 625-627.
- [3] N. Z. Bao, L. M. Shen, T. Takata and K. Domen, *Chem. Mater.*, 2008, **20**, 110-117.
- [4] R. Asahi, T. Morikawa, T. Ohwaki, K. Aoki and Y. Taga, *Science*, 2001, **293**, 269-271.
- [5] W. Morales, M. Cason, O. Aina, N. R. Tacconi and K. Rajeshwar, *J. Am. Chem. Soc.*, 2008, **130**, 6318-6319.
- [6] M. R. Hoffmann, S. T. Martin, W. Choi and D. W. Bahneman, *Chem. Rev.*, 1995, **95**, 6996.
- [7] Z. G. Zou, J. H. Ye, S. Kazuhiro and A. Hironori, *Nature*, 2001, **414**, 625-627.
- [8] R. Asahi, T. Morikawa, T. Ohwaki, K. Aoki and Y. Taga, *Science*, 2001, **293**, 269-271.
- [9] K. Maeda, K. Teramura, D. L. Lu, T. Takata, N. Saito, Y. Inoue and K. Domen, *Nature*, 2006, **440**, 295.
- [10] X. C. Wang, K. Maeda, A. Thomas, K. Takanabe, G. Xin, J. M. Carlsson, K. Domen and M. Antonietti, *Nat. Mater.*, 2009, **8**, 76-80.
- [11] (a) Z. G. Yi, J. H. Ye, N. Kikugawa, T. Kako, S. X. Ouyang, H. Stuart-Williams, H. Yang, J. Y. Cao, W. J. Luo, Z. S. Li, Y. Liu and R. L. Withers, *Nat. Mater.*, 2010, **9**, 559-564.
(b) Y. P. Bi, S. X. Ouyang, N. Umezawa, J. Y. Cao and J. H. Ye, *J. Am. Chem. Soc.*, 2011, **133**, 6490-6492.
- [12] X. X. Xu, C. Randorn, P. Efstathiou and J. T. S. Irvine, *Nat. Mater.*, 2012, **11**, 595-598.
- [13] (a) H. B. Fu, C. S. Pan, W. Q. Yao and Y. F. Zhu, *J. Phys. Chem. B*, 2005, **109**, 22432-22439; (b) Y. Tsunoda, W. Sugimoto and Y. Sugahara, *Chem. Mater.*, 2003, **15**, 632-635.
- [14] J. Wu, F. Duan, Y. Zheng and Y. Xie, *J. Phys. Chem. C*, 2007, **111**, 12866-12871.
- [15] F. Amano, K. Nogami, R. Abe and B. Ohtani, *J. Phys. Chem. C*, 2008, **112**, 9320-9326.
- [16] C. X. Xu, X. Wei, Y. M. Guo, H. Q. Wu, Z. H. Ren, G. Xu, G. Shen and G. R. Han, *Mater. Res. Bull.*, 2009, **44**, 1635-1641.
- [17] M. Shang, W. Z. Wang and H. L. Xu, *Cryst. Growth Des.*, 2009, **9**, 991-996.
- [18] L. S. Zhang, W. Z. Wang, Z. G. Chen, L. Zhou, H. L. Xu and W. Zhu, *J. Mater. Chem.*, 2007, **17**, 2526-2532.
- [19] Z. Chen, L. W. Qian, J. Zhu, Y. P. Yuan and X. F. Qian, *Cryst. Eng. Comm.*, 2010, **12**, 2100-2106.
- [20] X. F. Cao, L. Zhang, X. T. Chen and Z. L. Xue, *Cryst. Eng. Comm.*, 2011, **13**, 306-311.
- [21] L. Wu, J. H. Bi, Z. H. Li, X. X. Wang and X. Z. Fu, *Catal. Today*, 2008, **131**, 15-20.

- [22] Z. J. Zhang, W. Z. Wang, M. Shang and W. Z. Yin, *J. Hazard. Mater.*, 2010, **177**, 1013-1018.
- [23] S. B. Zhu, T. G. Xu, H. B. Fu, J. C. Zhao and Y. F. Zhu, *Environmental Science & Technology*, 2007, **41**, 6234-6239.
- [24] S. M. Lopez, M. C. Hidalgo, J. A. Navio and G. Colon, *Journal of Hazardous Materials*, 2011, **185**, 1425-1434.
- [25] M. S. Gui, W. D. Zhang, Y. Q. Chang and Y. X. Yu, *Chemical Engineering Journal*, 2012, **197**, 283-288.
- [26] Z. J. Zhang, W. Z. Wang, L. Wang and S. M. Sun, *ACS Appl. Mater. Interfaces*, 2012, **4**, 593-597.
- [27] J. X. Xia, J. Di, S. Y. H. Xu, J. Zhang, Y. G. Xu, L. Xu, H. M. Li and M. X. Ji, *RSC Adv.*, 2014, **4**, 82-90.
- [28] Q. C. Xu, D. V. Wellia, Y. H. Ng, R. Amal and T. T. Y. Tan, *J. Phys. Chem. C*, 2011, **115**, 7419-7428.
- [29] X. N. Li, R. K. Huang, Y. H. Hu, Y. J. Chen, W. J. Liu, R. S. Yuan and Z. H. Li, *Inorg. Chem.*, 2012, **51**, 6245-6250.
- [30] H. W. Huang, S. B. Wang, N. Tian and Y. H. Zhang, *RSC Adv.*, 2014, **4**, 5561-5567.
- [31] G. K. Fu, G. N. Xu, S. P. Chen, L. Lei and M. L. Zhang, *Catal. Commun.*, 2013, **40**, 120-124.
- [32] Y. Hu, Y. Liu, H. Qian, Z. Li and J. Chen, *Langmuir*, 2010, **26**, 18570-18575.
- [33] D. Jing and L. Guo, *J. Phys. Chem. C*, 2007, **111**, 13437-13441.
- [34] D. Barpuzary and M. Qureshi, *ACS Appl. Mater. Interfaces*, 2013, **5**, 11673-11682.
- [35] G. S. Li, D. Q. Zhang and J. C. Yu, *Environ. Sci. Technol.*, 2009, **43**, 7079-7085.
- [36] Y. X. Yu, W. X. Ouyang, Z. T. Liao, B. B. Du and W. D. Zhang, *ACS Appl. Mater. Interfaces*, 2014, **6**, 8467-8474.
- [37] Z. Fang, Y. F. Liu, Y. T. Fan, Y. H. Ni, X. W. Wei, K. B. Tang, J. M. Shen and Y. Chen, *J. Phys. Chem. C*, 2011, **115**, 13968-13976.
- [38] Y. W. Mi, S. Y. Zeng, L. Li, Q. F. Zhang, S. N. Wang, C. H. Liu and D. Z. Sun, *Mate. Res. Bull.*, 2012, **47**, 2623-2630.
- [39] M. R. Kim, Y. Kang and D. Jang, *J. Phys. Chem. C*, 2007, **111**, 18507-18511.
- [40] A. Ihs and B. Liedberg, *J. Colloid Interface Sci.*, 1991, **144**, 282-292.
- [41] N. Mahapatra, S. Panja, A. Mandal and M. Halder, *J. Mater. Chem. C*, 2014, **2**, 7373.

- [42] U. Srinivasan, P. A. Mieyal and J. J. Mieyal, *Biochemistry*, 1997, **36**, 3199-3206.
- [43] S. Y. Zeng, R. F. Tang, S. X. Duan, L. Li, C. H. Liu, X. L. Gu, S. S. Wang and D. Z. Sun, *Journal of Colloid and Interface Science*, 2014, **432**, 236-245.
- [44] L. Ge and J. Liu, *Materials Letters*, 2011, **65**, 1828-1831.
- [45] P. Tierno and W.A. Goedel, *J. Phys. Chem. B*, 2006, **110**, 3043-3050.
- [46] K. L. Zhang, C. M. Liu, F. Q. Huang, C. Zheng and W. D. Wang, *Appl. Catal. B: Environ.*, 2006, **68**, 125-129.
- [47] M. S. Gui, W. D. Zhang, Q. X. Su and C. H. Chen, *J. Solid State Chem.*, 2011, **184**, 1977-1982.
- [48] Giuseppe Marci, Vincenzo Augugliaro, Maria J. López-Muñoz, Cristina Martin, Leonardo Palmisano, Vicente Rives, Mario Schiavello, Richard J. D. Tilley and Anna Maria Venezia, *J. Phys. Chem. B*, 2001, **105**, 1026-1032.
- [49] A. Kudo, I. Tsuji and H. Kato, *Chem. Commun.*, 2002, **17**, 1958-1959.
- [50] L. Zhang, J. H. Yan, M. J. Zhou, Y. P. Yu, Y. Liu, and Y. N. Liu, *Trans. Nonferrous Met. Soc. China*, 2014, **24**, 743-749.
- [51] N. Li, L. Zhu, W. D. Zhang, Y. X. Yu, W. H. Zhang, and M. F. Hou, *Journal of Alloys and Compounds*, 2011, 509, 9770-9775.
- [52] G. K. Zhang, X. M. Ding, F. S. He, X. Y. Yu, J. Zhou, Y. J. Hu, and J. W. Xie, *Langmuir*, 2008, **24**, 1026-1030.
- [53] P. Sippel, D. Denysenko, A. Loidl, P. Lunkenheimer, G. Sastre and D. Volkmer, *Adv. Funct. Mater.*, 2014, **24**, 3885-3896.
- [54] D. N. Ke, T. Y. Peng, L. Ma, P. Cai and P. Jiang, *Appl. Catal. A*, 2008, **350**, 111-117.
- [55] L. Ren, J. Lei, J.B. Wang, M. Qiu and Y. Yu, *Nanotechnology*, 2009, **20**, 405602.
- [56] K. Vinodgopal, I. Bedja and P.V. Kamat, *Chem. Mater.*, 1996, **8**, 2180-2187.
- [57] S. Chatterjee, A.K. Tyagi and P. Ayyub, *J. Nanomater.*, 2014, **2014**, 1-7.
- [58] E. Forgacs, T. Cserhádi and G. Oros, *Environ. Int.*, 2004, **30**, 953-971.
- [59] S. Senthilkumaar, K. Porkodi, R. Gomathi, A. Geetha Maheswari and N. Manonmani, *Dyes Pigm.*, 2006, **69**, 22-30.
- [60] S. Ikeda, N. Sugiyama, S. Murakami, H. Kominami, Y. Kera, H. Noguchi, K. Uosaki, T. Torimoto, and B. Ohtani, *Phys. Chem. Chem. Phys.* 2003, **5**, 778-783.
- [61] B. Ohtani, R. M. Bowman, D. P. Colombo Jr., H. Kominami, H. Noguchi, and K. Uosaki, *Chem.*

Lett., 1998, **27**, 579-580.

[62] V.A. Sakkas, I.M. Arabatzis, I.K. Konstantinou, A.D. Dimou, T.A. Albanis and P. Falaras, *Appl. Catal. B: Environ.*, 2004, **49**, 195-205.

[63] H. Zhang and Y. F Zhu, *J. Phys. Chem. C*, 2010, **114**, 5822-5826.

[64] D. E. Dunstan, A. Hagfeldt, M. Almgren, H. O. G. Siegbahn, and E. Mukhtart, *J. Phys. Chem.*, 1990, **94**, 6197-6804.

[65] W. R. Becquerel, *J. Chem. Phys.*, 1960, **32**, 1505-1514.

[66] H. Gerischer, *Pure Appl. Chem.*, 1980, **52**, 2649-2667.

[67] H. Xu, J. Yan, Y.G. Xu, Y.H. Song, H.M. Li, J.X. Xia, C.J. Huang and H.L. Wan, *Appl. Catal. B: Environ.*, 2013, **129**, 182-193.

[68] Q.J. Xiang, J.G. Yu and M. Jaroniec, *J. Phys. Chem. C*, 2011, **115**, 7355.

[69] H.Q. Li, Y.M. Cui and W.S. Hong, *Appl. Surf. Sci.*, 2013, **264**, 581-588.

[70] (a) X. K. Li, and J. H. Ye, *J. Phys. Chem. C*, 2007, **111**, 13109-13116; (b) T. Watanabe, T. Takizawa, and K. Honda, *J. Phys. Chem.*, 1977, **81**, 1845-1851.

[71] (a) P. Qu, J. C. Zhao, T. Shen, H. Hidaka, and J. Mol, *Catal. A: Chem.*, 1998, **129**, 257-268; (b) T. X. Wu, G. M. Liu, J. C. Zhao, H. Hidaka, and N. Serpone, *J. Phys. Chem. B*, 1998, **102**, 5845-5851.

[72] P. Lei, C. Chen; J. Yang, W. Ma, J. Zhao, and L. Zang, *Environ. Sci. Technol.* 2005, **39**, 8466-8474.

[73] C. Chen, W. Zhao, J. Li, and J. Zhao, *Environ. Sci. Technol.*, 2002, **36**, 3604-3611.

[74] Y. Wang, K. Deng and L. Zhang, *J. Phys. Chem. C*, 2011, **115**, 14300-14308.